Poisson Effects on X-Ray Diffraction Patterns in Low-Temperature-Carburized Austenitic Stainless Steel

H. KAHN, G.M. MICHAL, F. ERNST, and A.H. HEUER

Austenitic stainless steel was carburized at low temperature to generate a hard surface layer. X-ray diffractometry (XRD) revealed that this "case" contained an expanded fcc lattice and significant residual stresses due to the interstitial carbon. The XRD patterns also exhibit consistent variations with crystallographic orientation. Using published elastic constants for austenitic stainless steel and appropriate approximations for the XRD elastic constants, the XRD peak position variations can be accounted for by orientation-dependent Poisson effects due to biaxial residual stresses. The XRD patterns of specimens containing either compressive or tensile residual stresses were consistent with this hypothesis.

I. INTRODUCTION

LOW-TEMPERATURE carburization (as well as low-temperature nitridation) of austenitic stainless steel results in improved properties, such as greatly increased surface hardness, wear resistance, fatigue resistance, and corrosion resistance.[1,2] The lattice parameter of the near-surface region is expanded by the interstitial carbon and nitrogen. X-ray diffractometry (XRD) of this so-called "expanded austenite" (also called S phase) has shown consistent variations in the observed lattice parameter, a_{hkl},

$$a_{hkl} = \frac{\lambda}{2\sin(\theta_{hkl})}(h^2 + k^2 + l^2)^{0.5} \qquad [1]$$

inferred from different peaks (hkl), where λ is the wavelength of the incident X-ray, and θ_{hkl} is the diffraction angle of peak (hkl). (Absent strain and assuming good sample alignment, a should be the same for any peak in an fcc material.) Typically, a_{200} is found to be larger than a_{111}, a_{220}, and a_{311}. Unfortunately, many researchers have only reported a few XRD peaks, rendering the investigation into the origin of this phenomenon difficult.

However, a recent study by Fewell and Priest[3] used synchrotron radiation to obtain diffraction information from low-temperature-nitrided 316 stainless steel up to the (640) peak. They thoroughly reviewed the possible mechanisms reported in the literature for the observed diffraction results, which are summarized next. A variation in the nitrogen content with grain orientation was discounted, because a_{hkl} did not depend on the X-ray angle of incidence. Tetragonal, monoclinic, and triclinic distortions were not considered, because they all involve peak splitting, which was not observed. The remaining possibilities included rhombohedral distortion, stacking faults, or lattice strain due to compressive residual stresses generated by the interstitial nitrogen. (The lattice parameter expansion in the case is impeded by the restraint imposed by the nontreated "core.")

Rhombohedral distortion does not involve peak splitting. The interplanar spacings, d_{hkl}, of a rhombohedral lattice are described by

$$\frac{1}{d_{hkl}^2} = \frac{(h^2 + k^2 + l^2)\sin^2\alpha_r + 2(hk + kl + hl)(\cos^2\alpha_r - \cos\alpha_r)}{a^2(1 - 3\cos^2\alpha_r + 2\cos^3\alpha_r)}$$

$$[2]$$

where a is the lattice parameter, and α_r is the rhombohedral angle. To obtain $a_{200} > a_{111}$, α_r must be greater than 90 deg, implying that $a_{220} > a_{311}$.

The XRD peak shifts due to stacking faults were first proposed by Warren[4] and later discussed in detail by Velterop et al.[5] Both analyses predict an increase in a_{200} and a decrease in a_{400} with increasing stacking fault density.

After carburization or nitridation, the interstitial carbon or nitrogen atoms will cause expansion of the lattice parameter, but as noted previously, compressive stresses will develop in the carburized or nitrided layer due to the constraint of the unaffected bulk of the steel specimen. The compressive stresses introduced by the interstitial solute will reduce the interplanar spacing of planes perpendicular to the surface of the carburized or nitrided layer. Since the compressive stresses are biaxial, corresponding Poisson expansion will occur in the direction of the surface. The degree of Poisson expansion will depend on the Miller indices of the various planes, due to the elastic anisotropy present, even in fcc crystals.

H. KAHN, Research Associate Professor, and G.M. MICHAL, F. ERNST, and A.H. HEUER, Professors, are with the Department of Materials Science and Engineering, Case Western Reserve University, Cleveland, OH 44106-7204. Contact e-mail: heuer@case.edu

While several other groups[6–8] have attempted to account for the effects of Poisson expansion on the XRD patterns of nitrided austenitic steels, Fewell and Priest[3] discounted the biaxial stress effect because they did not observe the predicted linear dependence of a_{200} or a_{400} on $\sin^2\psi$, where ψ is the tilt angle of the sample surface compared to $\psi = 0$ for the Bragg–Brentano setting ($\theta_{in} = \theta_{out}$). However, their data were obtained with several different X-ray angles of incidence, and the corresponding differences in X-ray penetration depths, along with a gradient in nitrogen concentration, could have affected their analysis. Fewell and Priest[3] concluded that no single explanation can successfully describe the XRD lattice parameter variations.

In this work, we arrive at different conclusions. We have investigated, in detail, the interplanar spacings and residual stresses of low-temperature carburized austenitic stainless steels using XRD. Using an analysis based on the most recent approximation for the X-ray elastic constants,[9] we find that the Poisson effect can explain the majority of the apparent XRD lattice parameter variations.

II. EXPERIMENTAL METHODS

Austenitic stainless steel specimens were treated by a gas-phase low-temperature paraequilibrium carburization process, described in more detail earlier,[1,10] at 460 °C for 24 hours to create a carburized case with a depth of ≈20 μm. Two different types of 316L austenitic stainless steel specimens were used: 6-mm-thick bulk specimens and 50-μm-thick foils. After carburization, thin layers were removed from the surface of some bulk 316L specimens *via* electropolishing. Bulk specimens (≈3-mm thick) of a different grade of austenitic stainless steel, REX 734, were also carburized. The nominal compositions of these two steels are listed in Table I.

Both carburized and nontreated specimens were examined by XRD with monochromated Cu K_α radiation in a Scintag X-1 diffractometer in the standard θ-θ Bragg–Brentano geometry. Surface carbon concentrations were measured using X-ray photoelectron spectroscopy (XPS) in a Perkin-Elmer PHI-5600 ultra-high vacuum system with a continuous inert gas sputtering source for sample cleaning, which was particularly important in removing superficial carbon. Samples were sputtered for 300 seconds (corresponding to ≈30 nm of material removal) before compositional analysis, to ensure removal of surface contaminants. The surface carbon concentration was also measured using glow-discharge optical emission spectrometry (GDOES) in a LECO* GDS-850A

---

*LECO is a trademark of LECO Corporation, St. Joseph, MI.

---

spectrometer, after a similar ≈50-nm material removal before making the measurement. A cross-sectional specimen was prepared from carburized bulk 316L, and the carbon concentration profile was measured with a PHI 680 scanning Auger microprobe (SAM), using an electron probe diameter of 50 nm. The SAM analysis was

Table I. Major Elements of the Studied Materials (Nominal Weight Percent)

Material	Fe	Cr	Ni	Mo	Mn	Si	Nb	N	Cu
316L	66.5	18	12	2.5	0.5	0.5	0	0	0
REX 734	61.7	21	10	2.5	3	0.8	0.5	0.3	0.2

performed with a constant low-flux Ar sputter to minimize contamination and calibrated with a series of Fe-C standards. A hardness profile was also taken of the metallographic cross-sectional specimen, using a Hysitron TriboScope nanomechanical test instrument (Minneapolis, MN).

III. RESULTS AND DISCUSSION

A. Bulk 316L

Figure 1 shows the hardness and carbon atomic fraction, X_C, profiles for the bulk carburized 316L specimen. The hardness and SAM composition data were taken from a cross-sectional specimen. The XPS and GDOES composition data were taken from the surfaces of an as-carburized specimen and carburized specimens that had been electropolished to remove 4-, 12-, 19-, 22-, and 27-μm-thick surface layers. The profiles indicate a carburized case depth of ≈20 μm.

Figure 2 shows XRD scans of bulk carburized 316L specimens, after removing 0-, 4-, 12-, and 27-μm-thick surface layers. The XRD scans of the samples with 19 and 22 μm removed from the case are very similar to the specimen with 27 μm removed and are not shown here for simplicity. For the specimens containing interstitial carbon (with 0, 4, or 12 μm of the case removed), the XRD peaks are observed at lower 2θ values, indicating the expected lattice parameter expansion. The lattice parameters determined from the peaks in this figure are plotted in Figure 3, assuming an fcc lattice. The systematic variations in lattice parameter determined
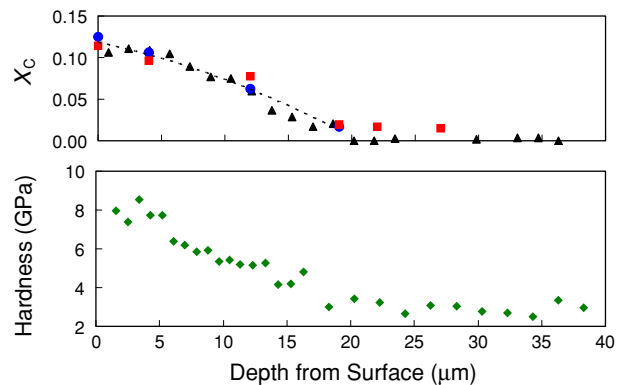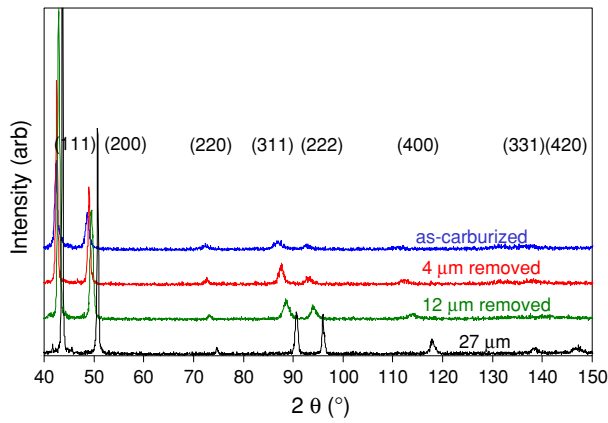

Fig. 1—Carbon concentration and hardness-depth profiles for a carburized 316L specimen. In the upper plot, the triangles, circles, and squares were obtained by SAM, XPS, and GDOES, respectively. The dashed line is a least-squares second-order polynomial fit to all the data within 20 μm of the original surface.

Fig. 2—XRD scans of bulk-carburized 316L specimens, as-carburized, and with 4-, 12-, and 27-μm-thick surface layers removed by electropolishing.
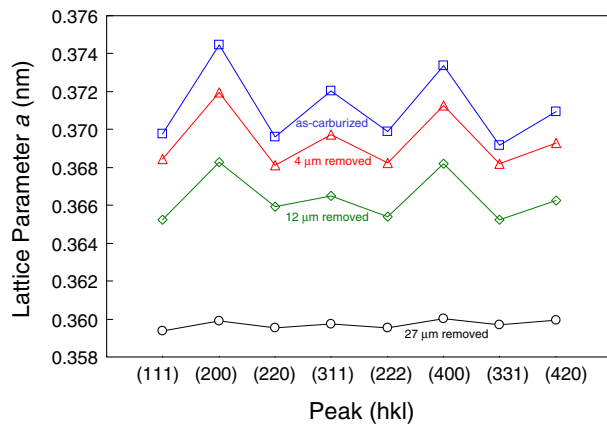

Fig. 3—Lattice parameters determined from the peaks in the XRD spectra in Figure 2. Open squares, triangles, diamonds, and circles represent the as-carburized, 4-μm removed, 12-μm removed, and 27-μm removed specimens, respectively.

from the individual XRD peaks are readily apparent in this plot. In all specimens, $a_{200} > a_{211}$ and $a_{311} > a_{220}$. These two inequalities occurring together eliminates rhombohedral distortion as the major origin of the lattice parameter variations. Also, both a_{200} and a_{400} display relatively large apparent lattice parameters, which discounts stacking faults as the primary origin of the systematic peak shifts.

To investigate the effects of Poisson expansion due to biaxial stresses, the residual stresses of all samples were determined using the standard XRD $\sin^2\psi$ technique.[11] The a_{420} values measured at various tilt angles, ψ, are shown in Figure 4. The residual stress, σ, is determined from this plot by

$$\sigma = \frac{\text{slope}}{\text{intercept}} \times \frac{2}{S2_{hkl}} \qquad [3]$$

where $S2_{hkl}$ is the hkl-dependent X-ray elastic constant. The value of $S2_{420}$ was calculated to be 0.01374 GPa^{-1} using the approximation of DeWit[9] and the elastic
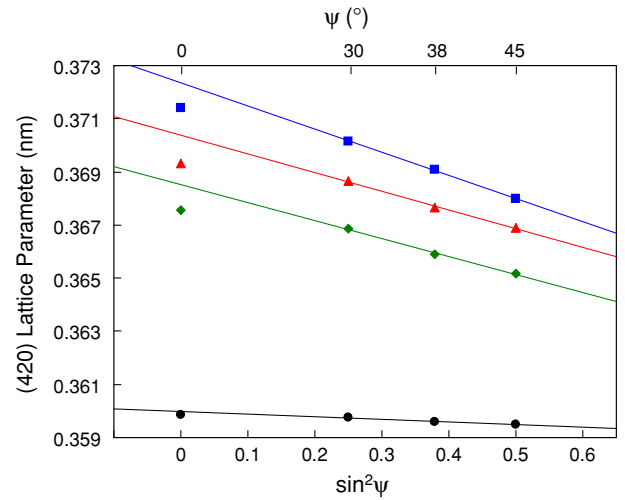

Fig. 4—XRD lattice parameters for the (420) peak as a function of $\sin^2\psi$. Filled squares, triangles, diamonds, and circles represent the as-carburized, 4-μm removed, 12-μm removed, and 27-μm removed specimens, respectively.

constants for a Fe-18 wt pct Cr-12 wt pct Ni alloy reported by Bradfield[12] ($c_{11} = 215.9$ GPa, $c_{12} = 144.6$ GPa, and $c_{44} = 128.9$ GPa). In Figure 4, for all four specimens, the a_{420} results for $\psi \geq 30$ deg fit well (Pearson correlation coefficient $R > 0.993$) to a straight line, but the results for $\psi = 0$ deg deviate from the fits. This is likely caused by the greater X-ray penetration at $\psi = 0$ deg, combined with the gradient in carbon concentration, creating an anomalously low value for a_{420}. This is similar to the "ghost stress" effect,[13] and therefore only the results for $\psi \geq 30$ deg are used to generate the best-fit lines in Figure 4. These lines reveal compressive stresses of 3.4, 2.8, 2.7, and 0.4 GPa for the as-carburized, 4-μm removed, 12-μm removed, and 27-μm removed specimens, respectively. This gradient in compressive stress is consistent with the X_C profile in Figure 1. The specimen with 27-μm removed specimens contains essentially no carbon and might be expected to contain no residual stress, but it does. This stress, however, is relatively small and may have arisen from damage resulting from specimen preparation.

The lattice parameters with Poisson effects removed were determined from the expression

$$a_{hkl} = \frac{a_{hkl,\sigma}}{1 + 2S1_{hkl}\sigma} \qquad [4]$$

where $a_{hkl,\sigma}$ is the lattice parameter containing stress effects (from Figure 3), and $S1_{hkl}$ is the hkl-dependent X-ray elastic constant, determined by the same approximation discussed previously[9] and listed in Table II. The biaxial stress-corrected lattice parameters are shown in the lower part of Figure 5. The systematic variations of Figure 3 are substantially reduced for all of the samples, particularly those with the lower carbon contents. The standard deviation of the lattice parameter variations for the most nonuniform specimen—the as-carburized specimen—is reduced from 0.0020 to 0.0007 nm.

Table II. Calculated Values for $S1_{hkl}$ ($\times 10^{-6}$ GPa^{-1})

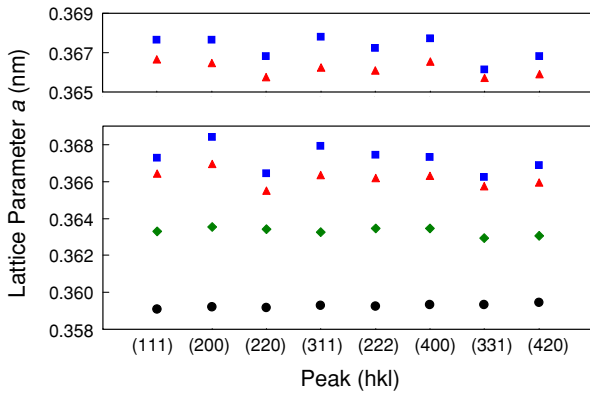| Alloy	(111)	(200)	(220)	(311)	(222)	(400)	(331)	(420)
316L	−990	−2419	−1271	−1644	−990	−2419	−1185	−1631
REX 734	−1010	−2540	−1310	−1700	−1010	−2540	−1210	−1690

Fig. 5—Lattice parameters from Figure 3, recalculated to remove the biaxial stress effects. Filled squares, triangles, diamonds, and circles represent the as-carburized, 4-μm removed, 12-μm removed, and 27-μm removed specimens, respectively. The upper graph shows the lattice parameters for the as-carburized and 4-μm removed specimens after correcting for stacking fault probabilities of 0.03 and 0.02, respectively.
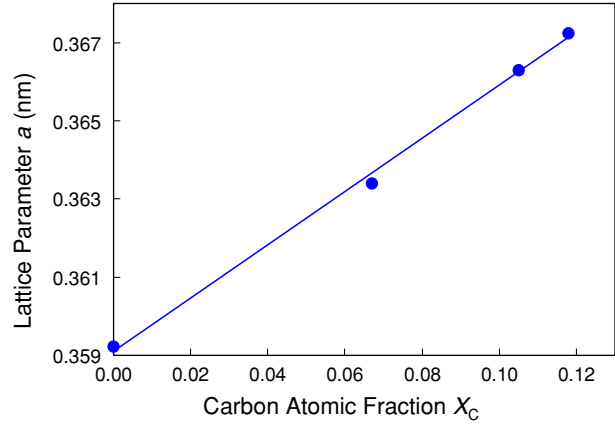

Fig. 6—Average lattice parameter as a function of X_C for carburized 316L specimens after compensating for biaxial residual stress. (For the linear least-squares fit, the Pearson correlation coefficient $R = 0.999$.)

It is possible that the carbon content affects the elastic constants, such that the values reported by Bradfield[12] are no longer valid. If the elastic constants are instead taken as fitting parameters, only a small improvement can be obtained. By decreasing c_{11} to 210 GPa (from 215.9 GPa), the standard deviation of the lattice parameter variations for the as-carburized specimen is reduced to 0.0006 nm.

The data in the upper part of Figure 5 show an attempt to further eliminate the lattice parameter variations by taking into account the effects of stacking faults. Warren's analysis[4] was used, assuming stacking fault probabilities of 0.03 and 0.02 (an average of one stacking fault for every 33 and 50 planes) for the as-carburized and 4-μm removed specimens, respectively. However, this only slightly lowers the standard deviation for the as-carburized specimen, to 0.0006 nm. Clearly, Poisson expansion due to the biaxial compressive residual stresses present after carburizing is the primary origin for the lattice parameter variations in Figure 3.

Figure 6 presents the average lattice parameters as a function of X_C after eliminating stress effects from Figure 5, using the best-fit line in Figure 1 for the X_C values. The linear fit in Figure 6 describes the relation

$$a(\text{after carburization}) = a(\text{beforecarburization}) + 0.068 X_C \qquad [5]$$

The da/dX_C factor of 0.068 nm is equivalent to 0.0028 nm/wt pct carbon. Previously reported values

for lattice expansion of austenite due to carbon range from 0.0033 (nm/wt pct)[14] to 0.0044 (nm/wt pct)[15] to 0.0054 (nm/wt pct),[16] but the highest value was determined from carburized specimens without accounting for stress effects,[16] and the experimental details were not described for the other two.[14,15] For comparison, if stress effects are not accounted for, the expansion factor suggested by our data is 0.0041 nm/wt pct ($da/dX_C = 0.10$ nm), an increase of nearly 50 pct in this constant.

B. 316L Foil

Specimens of 50-μm-thick 316L stainless steel foil were carburized for zero, one, or two 24-hour cycles. The XRD scans of these specimens are shown in Figure 7, and the lattice parameters determined from the peaks are shown by the open symbols in Figure 8. One minor complication for this measurement was that the foils were not completely flat, and so their surfaces did not lie at the precise eucentric point when loaded in the XRD apparatus. As a result, the peak positions became slightly shifted as a function of the diffraction angle 2θ, as demonstrated by comparing the × symbols and open circles in Figure 8 for the nontreated specimen. We compensated for this effect by assuming a height offset in the XRD apparatus, which caused the corrected XRD-determined lattice parameters to have an overall zero dependence on 2θ. The height offsets that satisfied this criterion were −0.3 mm, +0.7 mm, and +0.5 mm for the nontreated, 1 time carburized, and 2 times carburized specimens, respectively.

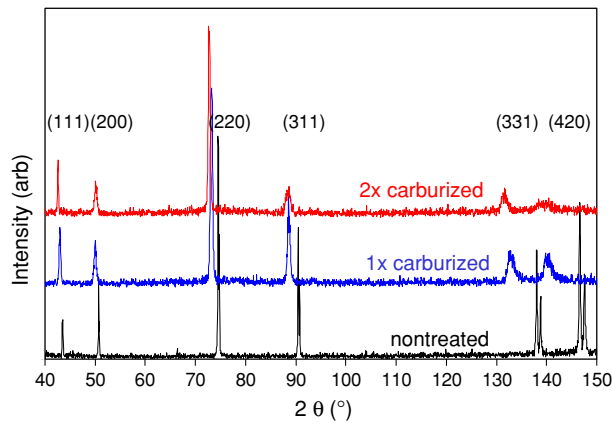Fig. 7—XRD scans of carburized and nontreated 316L foil specimens.
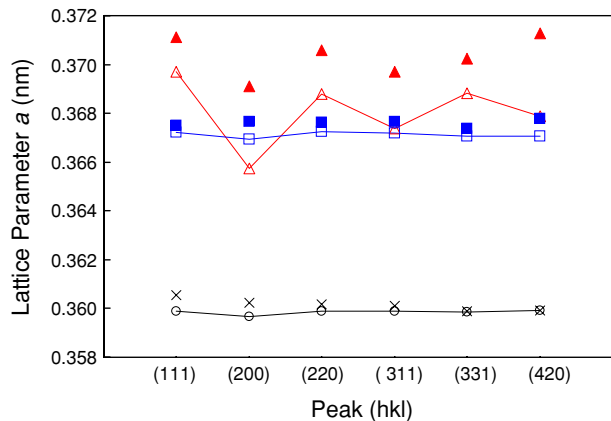

Fig. 8—Lattice parameters determined from the XRD peaks in Figure 7. × symbols represent noncorrected values for nontreated foil. Open triangles, squares, and circles represent the lattice parameters for 2 times carburized, 1 time carburized, and nontreated specimens, respectively, after correction for incorrect height in the XRD apparatus. Solid triangles and squares are the lattice parameters for 2 times carburized and 1 time carburized specimens, respectively, after compensating for biaxial residual stresses.

The crystallographic texture of the foil precluded detecting the (222) and (400) XRD peaks. The variations in the lattice parameters in Figure 8 are opposite to the variations seen in Figure 3, particularly for the 2 times carburized specimen, a result of the residual stresses being tensile, compared to the compressive residual stresses in the bulk sample. The residual stresses in the foil specimens were measured by the $\sin^2\psi$ technique to be 0, 0.4, and 1.9 GPa tensile, for the nontreated, 1 time carburized, and 2 times carburized specimen, respectively.

It seems counterintuitive that carburization can induce tensile residual surface stresses at the surface. However, the relatively small thickness of the foils allows the carbon to diffuse all the way to the center of the specimens. In the early stages of carburization, the near-surface regions on both sides of the foil expand due to the increased carbon content. The central region of the foil is thus subjected to high tensile stresses, which will be accommodated by plastic flow. In the later stages
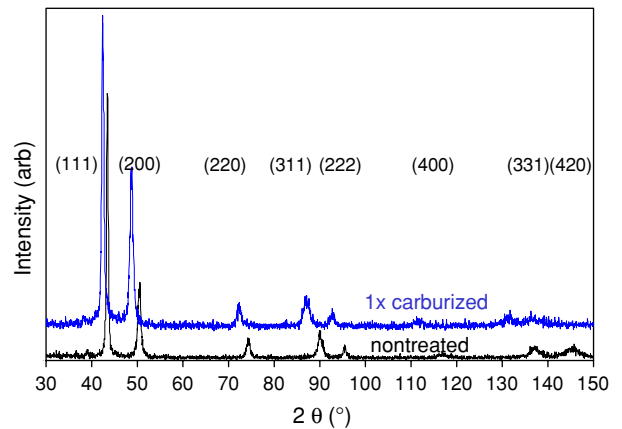

Fig. 9—XRD scans of carburized and nontreated REX 734 specimens.

of carburization, carbon diffuses into the central region of the foil, which consequently expands, inducing tensile stresses in the near-surface regions. Inasmuch as the near-surface regions already contain a significant carbon concentration, this raises the flow stress, and prevents the tensile stresses from being relieved.

Accounting for the Poisson effect due to the biaxial tensile stresses using Eq. [4] yields the lattice parameters shown by the filled symbols in Figure 8. Again, the lattice parameter variations are substantially diminished. The relationship [5] derived from bulk 316L predicts surface carbon atomic fractions of 0.11 and 0.15 for the 1 time carburized and 2 times carburized foil specimens, respectively. The XPS analysis revealed X_C to be 0.12 and 0.14, respectively, in satisfactory agreement.

Comparing the XRD results in Figures 2 and 7, it is clear that the textures of the bulk 316L and foil 316L specimens are significantly different. Yet, the consequences of the Poisson effect and the measured expansions per interstitial carbon atom are quite consistent. This validates two assumptions implicit to Eqs. [4] and [5]: (1) the in-plane biaxial stresses are uniform regardless of grain orientation, and (2) the interstitial carbon concentration does not depend on grain orientation.

C. REX 734

The 3-mm-thick specimens of REX 734 austenitic stainless steel, both nontreated and carburized, were studied. The XRD scans are shown in Figure 9, and the lattice parameters determined from the peaks are shown by the open symbols in Figure 10. The expected lattice expansion due to carbon and lattice parameter variations due to biaxial compressive stresses are evident. The stresses were determined by the $\sin^2\psi$ technique to be 0.6 and 2.9 GPa compressive, for the nontreated and carburized specimens, respectively. Using the DeWit approximation[9] and the elastic constants for a Fe-19 wt pct Cr-10 wt pct Ni alloy reported by Ledbetter[17] ($c_{11} = 205$ GPa, $c_{12} = 138$ GPa, and $c_{44} = 126$ GPa), $S2_{420}$ was calculated to be 0.0143 GPa^{-1}. The compressive stress in the nontreated specimen must have been introduced during specimen preparation. The calculated $S1_{hkl}$
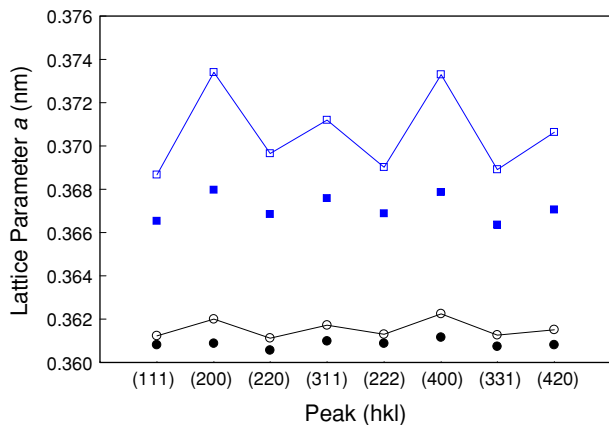
Fig. 10—Lattice parameters determined from the XRD peaks in Figure 9. Open squares and circles represent the lattice parameters for carburized and nontreated specimens, respectively. Solid squares and circles are the lattice parameters for carburized and nontreated specimens, respectively, after compensating for biaxial residual stresses.

values are shown in Table II. They vary from the 316L values by only a few percent at most. Equation [4] was used to compensate for the biaxial stresses, and the adjusted lattice parameters are shown by the filled symbols in Figure 10.

The apparent lattice parameter variations are largely, though not completely, eliminated. The standard deviation of the lattice parameter variations for the as-carburized specimen is reduced from 0.0019 to 0.0006 nm. One possible explanation for this incomplete correction is that the elastic constants taken for a Fe-19 Cr-10 Ni alloy may not be accurate for a REX 734 alloy with a very high interstitial carbon concentration. Although the interstitial carbon did not have an apparent effect on the elastic constants for 316L, when the elastic constants for the REX 734 are taken as fitting parameters, the lattice parameter variations can be practically eliminated by decreasing c_{11} to 195 GPa (from 205 GPa) and increasing c_{12} to 145 GPa (from 138 GPa). The standard deviation of the lattice parameter variations for the as-carburized specimen is reduced to 0.0002 nm. The stacking fault correction discussed previously cannot improve the lattice parameter consistency, because both a_{200} and a_{400} are relatively high, and the stacking fault correction would lower a_{200} while increasing a_{400}.

From the lattice expansion shown in Figure 10, the relationship in Eq. [4] predicts a surface X_C of 0.092. However, XPS analysis revealed 0.16, implying that $da/dX_C = 0.039$ nm. It is possible that the nitrogen content of the REX 734 steel produced effects on the relationship between the lattice parameter and carbon content.

IV. CONCLUSIONS

Low-temperature-carburized bulk specimens of 316L and REX 734 austenitic stainless steels revealed

expanded lattice parameters. The lattice parameters a_{hkl} determined from different XRD peaks exhibit systematic variations, with a_{111}, a_{220}, a_{222}, and a_{331} being relatively low, and a_{200}, a_{311}, and a_{400} relatively high. These variations are mostly eliminated by accounting for the crystallographic anisotropy in Poisson expansion due to the residual compressive stresses generated by carburization. In confirmation of this effect, carburized 316L foils also display lattice parameter expansion, but opposite variations in XRD-determined lattice parameter, due to tensile residual stresses generated by carburization. After compensating for the Poisson effect, the lattice expansion due to carbon is $da/dX_C = 0.068$ nm (0.0028 nm/wt pct) in 316L specimens and 0.039 nm (0.0016 nm/wt pct) for REX 734.

REFERENCES

1. G.M. Michal, F. Ernst, H. Kahn, Y. Cao, F. Oba, N. Agarwal, and A.H. Heuer: *Acta Mater.*, 2006, vol. 54, pp. 1597–1606.
2. S. Thaiwatthana, X.Y. Li, H. Dong, and T. Bell: *Surf. Eng.*, 2002, vol. 18, pp. 433–37.
3. M.P. Fewell and J.M. Priest: *Surf. Coat. Technol.*, 2008, vol. 202, pp. 1802–15.
4. B.E. Warren: *X-ray Diffraction*, Dover, New York, NY, 1990, pp. 275–91.
5. L. Velterop, R. Delhez, T.H. de Keijser, E.J. Mittemeijer, and D. Reefman: *J. Appl. Crystallogr.*, 2000, vol. 33, pp. 296–306.
6. Y. Sun, X. Li, and T. Bell: *J. Mater. Sci.*, 1999, vol. 34, pp. 4793–4802.
7. T. Christiansen and M.A.J. Somers: *Scripta Mater.*, 2004, vol. 50, pp. 35–37.
8. G. Abrasonis, J.P. Rivière, C. Templier, A. Declémy, L. Pranevicius, and X. Milhet: *J. Appl. Phys.*, 2005, vol. 97, pp. 083531-1–083531-10.
9. R. DeWit: *J. Appl. Crystallogr.*, 1997, vol. 30, pp. 510–11.
10. Y. Cao, F. Ernst, and G.M. Michal: *Acta Mater.*, 2003, vol. 51, pp. 4171–81.
11. B.D. Cullity: *Elements of X-ray Diffraction,* 2nd ed., Addison-Wesley, London, pp. 447–66.
12. G. Bradfield: *J. Iron Steel Inst.*, 1964, vol. 202, p. 616.
13. T. Christiansen and M. Somers: *Mater. Sci. Forum*, 2004, vols. 443–444, pp. 91–94.
14. R.C. Ruhl and M. Cohen: *Trans. TMS-AIME*, 1969, vol. 245, pp. 241–51.
15. C.S. Roberts: *Trans. AIME, J. Met.*, 1953, pp. 203–04.
16. Y. Sun, X. Li, and T. Bell: *Mater. Sci. Technol.*, 1999, vol. 15, pp. 1171–78.
17. H.M. Ledbetter: *Physica Status Solidi (a)*, 1984, vol. 85, pp. 89–96.